nature structural & molecular biology

Allosteric mechanism of water-channel gating by Ca^{2+}–calmodulin

Steve L Reichow[1,4], Daniel M Clemens[2,4], J Alfredo Freites[3], Karin L Németh-Cahalan[2], Matthias Heyden[3], Douglas J Tobias[3], James E Hall[2] & Tamir Gonen[1]

Calmodulin (CaM) is a universal regulatory protein that communicates the presence of calcium to its molecular targets and correspondingly modulates their function. This key signaling protein is important for controlling the activity of hundreds of membrane channels and transporters. However, understanding of the structural mechanisms driving CaM regulation of full-length membrane proteins has remained elusive. In this study, we determined the pseudoatomic structure of full-length mammalian aquaporin-0 (AQP0, *Bos taurus*) in complex with CaM, using EM to elucidate how this signaling protein modulates water-channel function. Molecular dynamics and functional mutation studies reveal how CaM binding inhibits AQP0 water permeability by allosterically closing the cytoplasmic gate of AQP0. Our mechanistic model provides new insight, only possible in the context of the fully assembled channel, into how CaM regulates multimeric channels by facilitating cooperativity between adjacent subunits.

CaM is a Ca^{2+}-binding protein that functions as a ubiquitous secondary messenger in several Ca^{2+} signaling pathways to dynamically regulate the function of hundreds of proteins. Many membrane proteins that act as transporters and channels, such as the cardiac and neuronal voltage-gated ion channels[1–4], the ryanodine receptor (RyR) family of Ca^{2+}-release channels[5–7], transient receptor potential channels[8–10], gap junctions[11–13] and the aquaporin water channels[14,15] are modulated by CaM in response to cytoplasmic Ca^{2+} fluctuations.

CaM is a small (16.7-kDa) bilobed protein composed of N- and C-terminal Ca^{2+}-binding domains connected by an internal flexible linker domain[16–19]. The N- and C-terminal lobes undergo structural rearrangements upon binding Ca^{2+} to expose a hydrophobic binding pocket that recognizes target proteins. This conformational change supports CaM's Ca^{2+}-dependent recognition mechanism, and its flexibility allows for binding to a diverse set of substrates. In addition, CaM is able to bind many of its cellular targets in its Ca^{2+}-free (apo) state, thus allowing for a constitutive interaction under low-Ca^{2+} conditions. In this way, CaM acts as an efficient signal transducer that can rapidly modulate the function of its target proteins with a dynamic response to changes in intracellular Ca^{2+} levels[20,21].

Aquaporins (AQPs) are a family of water channels, found in all kingdoms of life, that facilitate the flux of water molecules across membranes. Humans differentially express 13 AQP isoforms in a tissue-specific manner, with each isoform possessing unique substrate permeability characteristics and being regulated in different ways[22]. Structurally, AQPs are tetramers in which each monomer forms its own pore for water. Each monomer consists of six transmembrane helices that pack against one another as in a barrel, to form a hydrophilic pore for water permeation. Specificity for water involves the selectivity filter (constriction site I (CSI)) located at the extracellular vestibule. CSI constricts the water pore to a diameter of ~3 Å, which is large enough for water to pass through but is a steric barrier to larger molecules[23]. Further down the pore, roughly at its center, two Asn-Pro-Ala (NPA) motifs contribute a pair of asparagine residues to form the proton-exclusion site used to prevent the passage of protons[23,24]. The pore then expands to form the cytoplasmic vestibule. Although all AQPs share this transmembrane structure and pore architecture, the primary sequences of different AQPs vary greatly in their cytoplasmic N- and C-terminal domains, and these domains are often crucial for channel regulation.

AQP0 is a water channel that is exclusively expressed in the mammalian eye lens and whose permeability is directly modulated by CaM[25,26]. AQP0 serves a dual function in the lens by acting as a water channel[27–30] or as an adhesive protein mediating cell-cell adhesive junctions[31–33]. Regulation of water permeability by CaM is achieved through a Ca^{2+}-dependent interaction between Ca^{2+}–CaM and the cytoplasmic C-terminal domain of AQP0 (refs. 26,34,35). Typically, Ca^{2+}–CaM recognizes and binds its targets by wrapping around a single amphipathic helix. However, in the case of AQP0, Ca^{2+}–CaM interacts in a noncanonical fashion by simultaneously binding two AQP0 C-terminal helices to result in an overall 2:1 (AQP0/CaM) stoichiometry[35]. The functional consequence of Ca^{2+}–CaM binding to AQP0 is the inhibition of water permeation[26,35], although the mechanism by which this occurs is poorly understood.

Despite the importance of CaM regulation in membrane protein biology, there are currently no structural models for any full-length membrane protein channel in complex with CaM. Instead, numerous structures of CaM bound to fragments of membrane proteins

[1]Howard Hughes Medical Institute, Janelia Farm Research Campus, Ashburn, Virginia, USA. [2]Department of Physiology and Biophysics, University of California, Irvine, Irvine, California, USA. [3]Department of Chemistry, University of California, Irvine, Irvine, California, USA. [4]These authors contributed equally to this work. Correspondence should be addressed to J.E.H. (jhall@uci.edu) or T.G. (gonent@janelia.hhmi.org).

Received 4 April; accepted 5 June; published online 28 July 2013; doi:10.1038/nsmb.2630

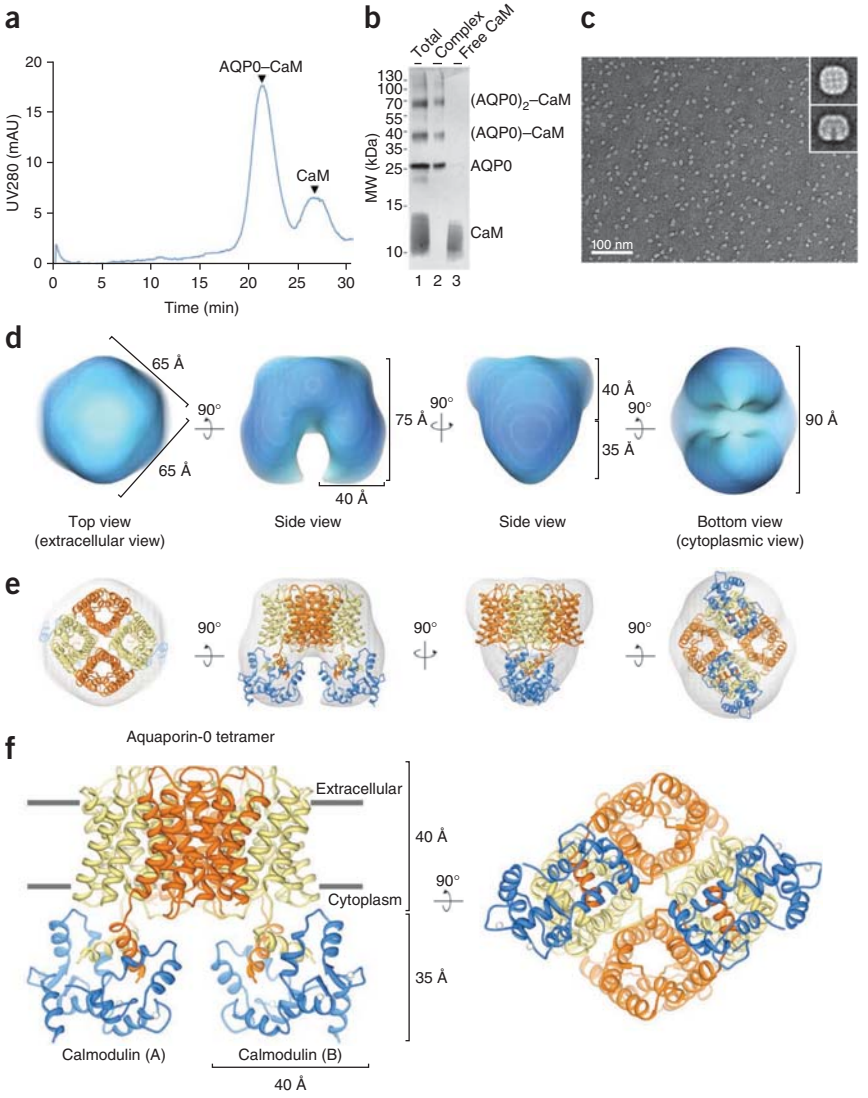

Figure 1 Purification and pseudoatomic model of the AQP0–CaM complex determined by EM. (**a**) Chromatogram showing purification of the AQP0–CaM cross-linked complex from excess free CaM by size-exclusion chromatography. mAU, milliabsorbance units. (**b**) Silver-stained SDS-PAGE showing fractions from the size-exclusion chromatography purification. Lane 1, total starting material; lane 2, purified AQP0–CaM cross-linked complex, dissociated in SDS into three protein bands migrating at 26, 39 and 65 kDa, corresponding to the AQP0 monomer, the 1:1 AQP0–CaM cross-link and the 2:1 $(AQP0)_2$–CaM cross-link, respectively; lane 3, free CaM migrating as a diffuse band at ~13 kDa. (**c**) Electron micrograph of negatively stained AQP0–CaM particles. Inset, symmetrized projection averages of the AQP0–CaM complex. (**d**) Different views of the 3D reconstruction of the AQP0–CaM complex. (**e**) Fitting of the crystallographic structures of AQP0 (orange and yellow) and CaM (blue) into the 3D reconstruction (gray mesh). (**f**) Pseudoatomic model of the AQP0–CaM complex displaying two CaM molecules (A and B) bound to the cytoplasmic C-terminal helices of the AQP0 tetramer.

exist, and these are typically of small ~20 residue peptides or domains of the channel in complex with CaM[36–39]. This is because full-length channels are often difficult to work with, and their associations with CaM can be transient and mediated by flexible domains refractory to structural analysis. Cryo-EM reconstructions of the RyR in complex with CaM have been reported previously[40,41]; however, an absence of high-resolution structural information for the RyR channel has prevented a mechanistic understanding of CaM regulation, and no pseudoatomic model of the complete complex has been obtained. Because of these difficulties and the lack of information from numerous systems, it became clear that hybrid techniques are required to yield a structural model of CaM bound to a full-length channel, to allow preliminary understanding of how CaM dynamically modulates channel function.

To gain a mechanistic understanding of how CaM is used to modulate the water permeability of AQP0, we used EM, structural modeling, molecular dynamics and functional mutation studies to develop a pseudoatomic structure of the full-length AQP0 in complex with CaM. Our structural model allowed us to dissect the mechanism by which CaM dynamically modulates AQP0 water-channel permeability, and in turn, we tested this experimentally by mutagenesis and permeability studies. This work provides the first structural model, to our knowledge, of CaM bound to any full-length channel. Our mechanistic model provides new insights into the role of cooperativity in regulating AQPs and offers cues into how CaM allosterically modulates the functions of other membrane channels.

RESULTS

Pseudoatomic model of the AQP0–calmodulin complex

Native AQP0 and recombinant CaM were purified to homogeneity, and the complex was formed in the presence of calcium, as previously described[35]. We stabilized the AQP0–CaM complex for EM studies, using the zero-length cross-linking reagent 1-ethyl-3-(3-dimethylaminopropyl) carbodiimide (EDC), and effectively separated AQP0–CaM cross-linked complex from excess CaM by size-exclusion chromatography (**Fig. 1a**,**b**). The purified complex eluted as a monodispersed species with a retention time consistent with the fully assembled AQP0–CaM complex and comprised an AQP0 tetramer in a detergent micelle in complex with two CaM molecules (**Fig. 1a**). We assessed the peak fraction by denaturing SDS-PAGE, which identified three species with apparent molecular weights of ~26 kDa, ~39 kDa and ~65 kDa corresponding to the AQP0 monomer, the 1:1 AQP0–CaM cross-link and the 2:1 $(AQP0)_2$–CaM cross-link, respectively (**Fig. 1b** and **Supplementary Fig. 1**).

Upon negative staining and EM visualization of purified AQP0–CaM complex, the AQP0–CaM complexes appeared as homogeneous particles ~7 nm in size and were evenly distributed on the EM grid (**Fig. 1c**). Projection averages revealed predominant views consisting of square-shaped structures (**Fig. 1c**) and views containing distinctive bilobed features, interpreted as side views (**Fig. 1c**). We calculated an initial three-dimensional (3D) reconstruction from the tilted-pair data set by random conical methods[42] and further refined with FREALIGN[43] to produce a final ~25-Å reconstruction (**Fig. 1d**).

The 3D reconstruction of the AQP0–CaM complex shows a bilobed structure consisting of a square-shaped domain with two protrusions extending off the face of the main body. The square-shaped domain is 65 × 65 Å when viewed from the 'top' of the reconstruction (**Fig. 1d**). This top view is consistent with the square-shaped views that we observed in projection averages (**Fig. 1c**). Rotation of the map 90° along the *x* axis gives a side view of the reconstruction that stands at 75 Å tall and reveals the two lobes extending from the main domain, each 40 Å wide and 35 Å tall (**Fig. 1d**). These features correspond well with the bilobed features observed in the projection averages (**Fig. 1c**). The main square-shaped domain is 40 Å tall when viewed from the side (**Fig. 1d**). An additional 90° rotation along the *x* axis displays the 'bottom' of the reconstruction, showing the two lobes of the EM map oriented toward the reader and separated by a cleft ~10–15 Å wide (**Fig. 1d**). In this work, we refer to the top and bottom as the extracellular and cytoplasmic views, respectively.

We used the EM map to guide the construction of a pseudoatomic model of AQP0 in complex with CaM (**Fig. 1e**,**f** and **Supplementary Fig. 2**). The crystal structure of the AQP0 tetramer (PDB 2B6P)[30] fit well into the main body of the EM map (65 × 65 × 40 Å), whereas CaM fit well into the two lobe features seen in side views of the particles (40 × 35 Å). The AQP0 tetramer was placed with its cytoplasmic side facing the lobe features of the EM map. We used Chimera[44] to computationally minimize the initial fitting (**Fig. 1e**).

We previously demonstrated that CaM binds two cytoplasmic AQP0 C-terminal helices simultaneously[35]. The only conformational arrangement that facilitated this binding mode in the AQP0 tetramer was for two neighboring C-terminal helices to come together in an antiparallel fashion. Of the >200 CaM complexes currently deposited in the Protein Data Bank (http://www.rcsb.org/), there are only two structures of Ca^{2+}–CaM bound to two adjacent antiparallel helices. These belong to the plant glutamate decarboxylase (ptGAD)–CaM complex[45] and the voltage-gated calcium channel ($Ca_{V1.2}$)–CaM complex[46,47]. Only the compact structure of the ptGAD–CaM complex fit well within the lobes of 40 × 35 Å in the EM reconstruction (**Fig. 1e**). We modeled the cytoplasmic C-terminal α-helices of AQP0 (residues 227–241) by using the antiparallel ptGAD α-helices as templates. The α-helices were connected to the transmembrane domain of AQP0 by short linker domains (residues 223–226) (Online Methods and **Supplementary Fig. 2**). The resulting pseudoatomic model of the AQP0–CaM complex contains the two Ca^{2+}–CaM molecules located directly beneath two of the AQP0 subunits and bound to the C-terminal helices of adjacent monomers (**Fig. 1f**). After energy minimization, the final model displayed no steric clashes, and a calculated map at 25 Å yielded a cross-correlation of 0.95 when compared to the experimental map.

Calmodulin uses a hydrophobic 'bind-and-capture' mechanism

The AQP0 CaM-binding domain ($AQP0^{CBD}$) contains an α-helix with several highly conserved hydrophobic residues that could be recognized by the hydrophobic N- and C-lobe binding pockets in Ca^{2+}–CaM (**Fig. 2a**). To determine which of these residues are involved in CaM recognition, we mutated each individual site to alanine and characterized the thermodynamic effects on binding to CaM, using isothermal titration calorimetry (ITC) (**Fig. 2a–c** and **Supplementary Fig. 3**).

ITC studies used 20-residue peptides corresponding to the bovine $AQP0^{CBD}$ sequence shown in **Figure 2a**. The wild-type $AQP0^{CBD}$, when mixed with CaM, produced large heats of binding that fit well to a two-state binding model (**Fig. 2b**). The stepwise binding showed an initial high-affinity event with an association constant (K_{a1} of ~1.4×10^7 M^{-1}) followed by a second lower-affinity binding event (K_{a2} of ~7.8×10^4 M^{-1}). Fitting of the energetic parameters to a two-state binding model yielded an overall free energy (ΔG_{1+2}) equal to −16.4 kcal mol^{-1}. (**Supplementary Fig. 3** contains a full table of thermodynamic parameters obtained by ITC.) Each of the $AQP0^{CBD}$ mutations resulted in unique thermodynamic effects on binding to CaM (**Fig. 2c**). Mutations L227A and V230A resulted in the largest overall energetic penalties, $\Delta\Delta G_{1+2}$ of 8.4 kcal mol^{-1} and 7.75 kcal mol^{-1}, respectively. Only a 1:1 stoichiometric complex was formed with CaM and these two mutant peptides, in contrast to the 2:1 stoichiometry displayed by the wild-type $AQP0^{CBD}$ (**Fig. 2c**). Hydrophobic-residue mutations L234A and L237A also showed reduced binding affinity compared to that of wild type, but these mutants could maintain a 2:1 complex with CaM. The L234A mutation resulted in an ~83% reduction in K_{a1} and a 38% reduction in K_{a2} (**Fig. 2c**), with an overall $\Delta\Delta G_{1+2}$ of 1.3 kcal mol^{-1}. The L237A mutation showed a 63% reduction in K_{a1}, whereas K_{a2} was essentially unaffected (**Fig. 2c**) and resulted in an overall $\Delta\Delta G_{1+2}$ of 0.5 kcal mol^{-1}. Notably, mutation of Ile236 to alanine produced an enhanced binding energy $\Delta\Delta G_{1+2}$ of −0.87 kcal mol^{-1}. This enhanced affinity is primarily due to a more favorable interaction during the second binding event (K_{a2}) that was increased by ~410% over wild type (**Fig. 2c**).

To assess the structural context of these mutational effects, we mapped the $AQP0^{CBD}$ residues to a two-dimensional helical-wheel representation (**Fig. 2d**). Notably, the hydrophobic residues that resulted in energetic penalties upon mutation to alanine (Leu227, Val230, Leu234 and Leu237) all cluster along the same face of the $AQP0^{CBD}$ α-helix. In contrast, the residue Ile236 that resulted in an enhanced binding affinity when mutated to alanine is located on the opposing side of the α-helix, which is characterized by a mixture of hydrophilic residues (**Fig. 2d**). This analysis suggests that it is this hydrophobic face of the $AQP0^{CBD}$ that interacts with the N- and C-lobe binding pockets of CaM during complex formation. In our structure of the AQP0–CaM complex, the $AQP0^{CBD}$ domains are modeled with the hydrophobic faces displayed toward the N- or C-lobe binding pockets of CaM (**Fig. 2e**) while the hydrophilic face is primarily solvent exposed.

In the CaM–free AQP0 crystal structure, the C-terminal α-helices of AQP0 are positioned beneath each monomer and stabilized in this orientation, in part, by van der Waals interactions formed between the hydrophobic $AQP0^{CBD}$ residue Leu237 and the cytoplasmic-loop residue Leu83 (ref. 30). For CaM to bind AQP0, this interaction must be broken to allow the C termini of neighboring monomers to rotate and come together to form the antiparallel configuration that is stabilized by CaM. Our binding studies suggest that this configuration is stabilized by CaM through a stepwise bind-and-capture mechanism driven by hydrophobic interactions. The initial high-affinity 1:1 binding interaction would allow CaM to bind the AQP0 tetramer in the absence of a preformed antiparallel configuration between neighboring $AQP0^{CBD}$ domains (**Fig. 2f**). Once a 1:1 complex is formed, the proximity of a neighboring $AQP0^{CBD}$ domain would allow CaM to readily capture a second $AQP0^{CBD}$ in the antiparallel arrangement (**Fig. 2f**). The mutations studied here revealed distinct energetic contributions for each binding event, a result suggesting that these hydrophobic sites participate in separate and unique roles during this two-step bind-and-capture mechanism for forming the AQP0–CaM complex.

Calmodulin stabilizes AQP0 and closes the channel gate

There are several mechanisms by which CaM binding to the AQP0 C terminus could inhibit water-channel permeability. In our

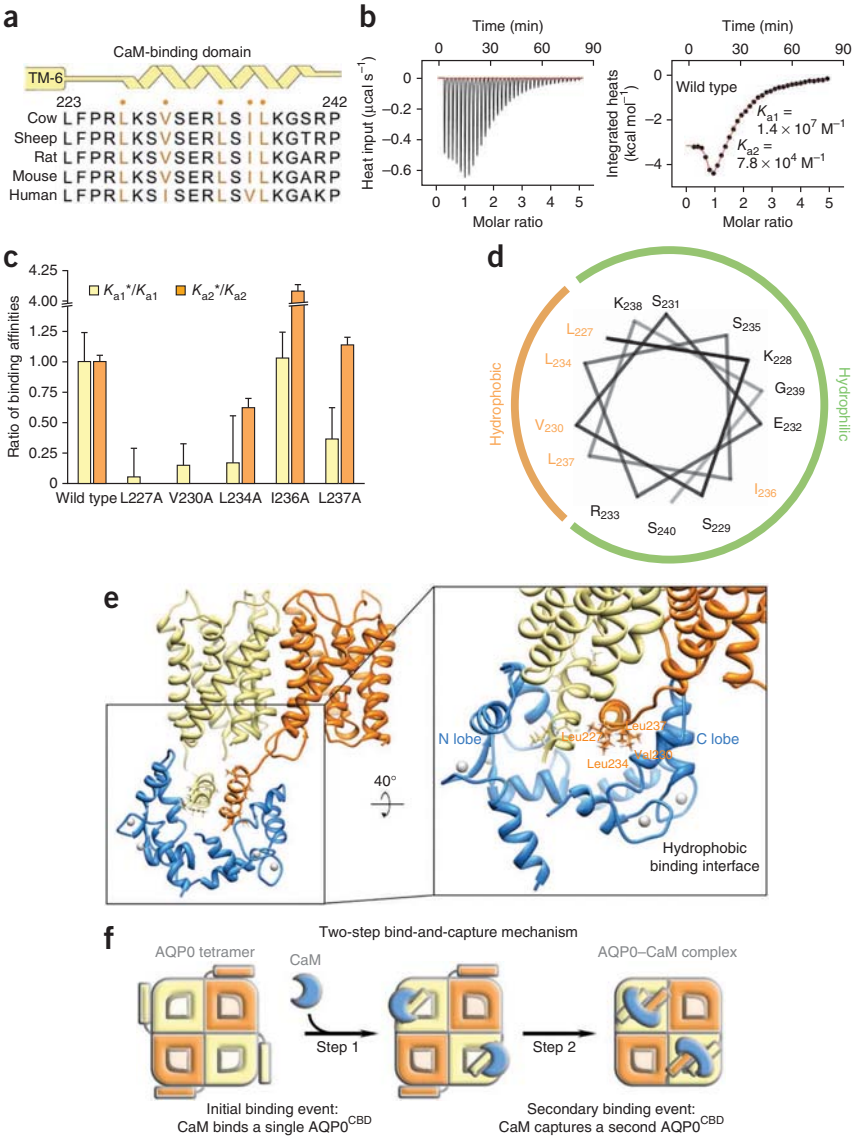

Figure 2 Hydrophobic interactions involved in AQP0–CaM complex formation. (**a**) Schematic of the secondary structure (yellow) and primary-sequence alignment of the AQP0 calmodulin-binding domain ($AQP0^{CBD}$). Residues in orange (and marked by dots) indicate conserved hydrophobic residues within the α-helical $AQP0^{CBD}$. (**b**) Left, ITC raw heats of binding of Ca^{2+}–CaM to the wild-type $AQP0^{CBD}$ peptide. Right, binding isotherm fit with a two-state binding model. (**c**) Ratio of binding affinities obtained by ITC for $AQP0^{CBD}$ peptides when each hydrophobic site (orange in **a**) was mutated to alanine. Ratios are calculated as mutant (K_a^*) over wild-type K_a values. Error bars indicate uncertainties following χ^2 minimization of the fitted binding models. (**d**) Helical-wheel analysis identifying a hydrophobic face involved in CaM recognition. (**e**) Structure of AQP0–CaM showing two AQP0 monomers bound to CaM (colored as in **Fig. 1**). Zoom view shows the $AQP0^{CBD}$ (yellow and orange helices) with AQP0 residues forming the proposed hydrophobic interface, with CaM shown as stick representations. (**f**) Schematic illustrating the two-step bind-and-capture mechanism for assembly of the 2:1 AQP0–CaM complex.

structural model of the AQP0–CaM complex, the two CaM molecules are positioned directly below the cytoplasmic pores of two of the four AQP0 monomers (**Figs. 1f** and **2f**). This arrangement suggested that CaM could potentially act as a plug[35]. However, 3D water density and pore profile analysis with HOLE[48] show that the cytoplasmic vestibule of these subunits could remain open and accessible to bulk water even when CaM is bound (**Fig. 3a**,**b**). Therefore, to gain insight into the change in the channel conformational dynamics that occurs when CaM is bound, we conducted a comparative molecular dynamics study on the CaM-free and CaM-bound AQP0 tetramer. The starting points of the two simulations contained identical conformations of the AQP0 tetramer in a palmitoyl-oleoyl-phosphatidylcholine (POPC) lipid bilayer with or without the two CaM molecules (**Supplementary Fig. 4**). After equilibration of the two systems, the two molecular dynamics simulations ran for ~500 ns.

The calculated single-channel water permeability (p_f) for the CaM-free AQP0 tetramer was 2.1×10^{-15} ($\pm 1.8 \times 10^{-15}$ s.e.m. of the four pores from each trajectory) $cm^3\ s^{-1}$ (ref. 49), consistent with previous molecular dynamics and functional studies[28,50–52]. In the CaM-bound AQP0 simulation, p_f values within the tetramer were reduced, to as low as $0.035 \times 10^{-15}\ cm^3\ s^{-1}$. These results are in line with our previous functional studies showing that CaM binding to AQP0 results in water-channel inhibition[14,26]. To gain further insight into the mechanism of water-channel inhibition, we assessed the conformational dynamics of AQP0 by the per-residue α-carbon r.m.s. fluctuations (**Fig. 3c–e**). Clustering analysis of r.m.s. fluctuations shows that CaM binding limits the overall dynamics of each of the AQP0 monomers in the tetramer. The highest r.m.s. fluctuation values in the CaM–free system mapped to the extracellular loops and the cytoplasmic C terminus, the site of CaM binding, whereas residues within the transmembrane domain exhibited low thermal fluctuations (**Fig. 3c**,**d**). These results are in agreement with the experimental temperature factors obtained by electron crystallography of AQP0 in a lipid membrane[30].

Unlike most other aquaporins, AQP0 has a channel pore containing a second constriction site, termed CSII, located at the cytoplasmic vestibule of the channel[33]. Residues forming CSII were among the most dynamic during the CaM-free molecular dynamics simulation (**Fig. 3d**). In the CaM-bound simulation, the r.m.s. fluctuations of the AQP0 C-terminal α-helices were markedly reduced when confined by CaM (**Fig. 3e**). In addition, the most stabilized residues mapped to the base of the last transmembrane helix (TM6) and to residues forming CSII (**Fig. 3e**). These results indicate that CaM constrains the dynamics of AQP0, particularly by stabilizing the CSII region.

Stabilization of the AQP0 CSII in the CaM-bound molecular dynamics simulation was notable because this site has been proposed to act as a dynamic channel gate[33,50]. The conserved residues Phe75, His66 and Tyr149 form CSII in AQP0 (**Fig. 4a**,**b**). Tyr149 displayed large movements during the time course of the simulations.

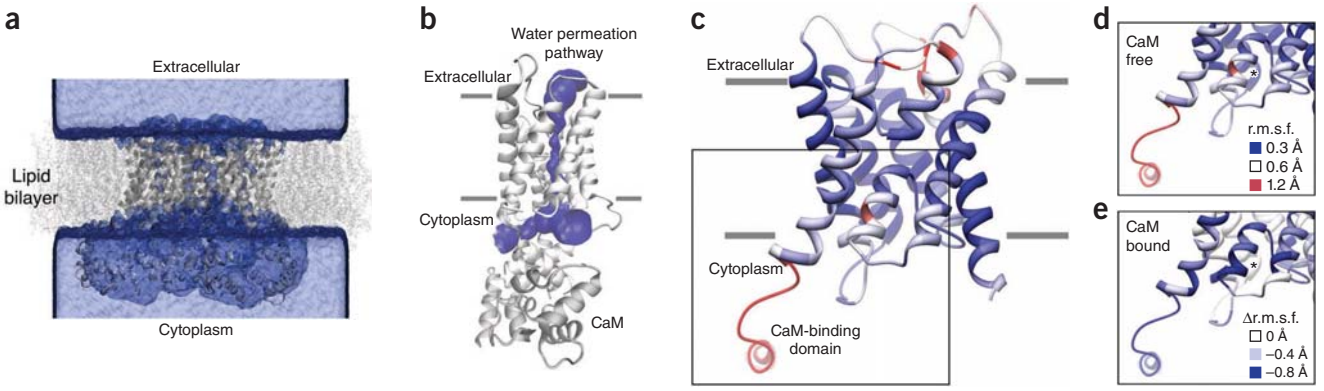

Figure 3 Calmodulin restricts the dynamics of AQP0. (**a**) Water density (blue isosurface) for the equilibrated AQP0–CaM (gray ribbon) in a lipid bilayer (gray stick). (**b**) Pore profile analysis with HOLE[48] showing water permeation pathway (blue surface) in the CaM-bound conformation of the AQP0 protomer (white and gray ribbon). (**c**) CaM-free per-residue r.m.s. fluctuation (r.m.s.f.) values mapped to the AQP0 structure according to color (blue, 0.3 Å; white, 0.6 Å; red, 1.2 Å). (**d**) Zoom view of the cytoplasmic domain of AQP0. (**e**) Change in protein dynamics (Δr.m.s.f.) of the CaM-bound system compared to the CaM-free system mapped to the AQP0 structure according to color (white, 0 Å; light blue, –0.4 Å; dark blue, –0.8 Å). Asterisks in **d** and **e** indicate the position of the AQP0 cytoplasmic constriction site II (CSII).

The side chain conformation oscillated between a downward 'open' orientation (**Fig. 4b**) and an upward 'closed' orientation (**Fig. 4b** and **Supplementary Video 1**). The difference in pore diameter between the open and closed states was ~2.5 Å, and in the closed orientation Tyr149 narrowed the pore diameter at CSII to ~1.5 Å (**Fig. 4c**). This tight closure would effectively block the passage of water molecules.

To assess the differences in the dynamics at CSII for the AQP0–CaM complex, we monitored the distance between Tyr149 and the opposed residue Phe75 over the time course of the two simulations (**Fig. 4d**). In the CaM-free system, the distance between these residues varied between ~3.5 Å and 12 Å, with a main distribution centered at 6.6 Å and a second smaller population centered at 9 Å (**Fig. 4d**). In the CaM-bound system, the distance between the residues shifted more toward pore closure (**Fig. 4d**). The CaM-bound system also exhibited a major population centered at 6.4 Å, but in addition, we observed a new population of structures with shorter inter-residue displacement (**Fig. 4d**). Furthermore, the population of structures centered at the large 9-Å displacement in the CaM-free system was essentially absent in the CaM-bound system. This analysis indicated that the probability of CSII adopting a closed state increases in the presence of CaM.

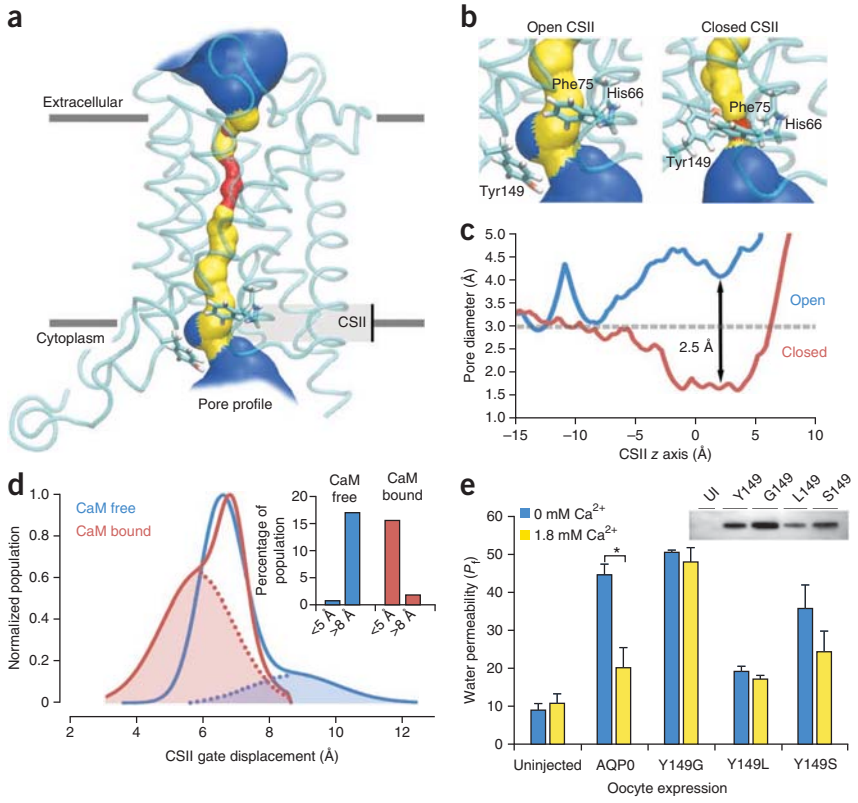

Figure 4 CaM binding closes the AQP0 cytoplasmic constriction site gate II (CSII). (**a**,**b**) Structures illustrating pore profile analysis of AQP0 during the molecular dynamics simulation. Tyr149 is shown in a downward, open conformation (**a**; **b**, left) and in an upward, closed conformation (**b**, right). The location of CSII is indicated in **a**. Side chains of the CSII residues Tyr149, Phe75 and His66 are displayed as sticks. (**c**) Plot indicating the pore diameter of the open AQP0 CSII (blue) and the closed CSII (red). (**d**) Plot indicating the population of structures obtained during the CaM-free AQP0 (blue) and CaM-bound AQP0 (red) molecular dynamics simulations, clustered according to the displacement of their CSII residues Tyr149 and Phe75. Inset, plot showing the population of structures with CSII displacement <5 Å or >8 Å. (**e**) Water channel permeability rates (P_f; μm s^{-1}) obtained from oocytes expressing wild-type AQP0 and CSII mutants (Y149G, Y149L and Y149S) obtained under buffer conditions of 0 mM (blue) or 1.8 mM Ca^{2+} (yellow). The AQP0 P_f is significantly inhibited by Ca^{2+} ($P = 0.012$ by two-sided t test ($n = 10$ biological replicates)). Inset, anti-AQP0 immunoblot verifying that each construct was expressed and correctly trafficked to the plasma membrane (uncropped immunoblot in **Supplementary Fig. 5**).

Mutation of the AQP0 gate abolishes Ca^{2+}–CaM regulation

Our molecular dynamics results indicated that Ca^{2+}–CaM binding to the AQP0 C terminus causes a shift in the equilibrium between the open and closed states of the channel. This result suggested an intimate relationship between CaM binding to the C terminus of AQP0 and the conformational dynamics of the conserved residues forming the CSII gate. If this relationship is indeed present, mutation of the CSII residues should abrogate Ca^{2+}–CaM regulation of water-channel permeability. To test this hypothesis, we assayed bulk water-channel permeability rates of wild-type AQP0 and various AQP0 CSII point mutants by monitoring cell swelling of *Xenopus laevis* oocytes under varying calcium concentrations.

When calcium was removed from the buffer (0 mM Ca^{2+} with 2 mM EGTA), oocytes expressing wild-type AQP0 exhibited bulk water permeability rates (P_f) of $44.6 \times 10^{-5} \pm 2.8 \times 10^{-5}$ μm s^{-1} (± s.e.m.; $n = 10$), well above those of control cells (**Fig. 4e**). In the presence of high calcium (1.8 mM Ca^{2+}), the rate of water-channel permeability was approximately halved ($P_f = 20.2 \times 10^{-5} \pm 5.2 \times 10^{-5}$ μm s^{-1} (± s.e.m.); $P = 0.012$ by two-sided t test ($n = 10$ biological replicates)), consistent with previous experimental results[14,26]. This effect has previously been shown to be CaM dependent[14].

Our molecular dynamics studies suggested that Tyr149 acts as the dynamic gating residue at CSII. When this residue was mutated either to a glycine, leucine or serine, the channels maintained their ability to facilitate water flux; however, they lost the ability to respond to high-calcium conditions. In the Y149G mutant, as compared to wild type, channels displayed increased water permeability rates (at low calcium) ($P_f = 50.6 \times 10^{-5} \pm 0.5 \times 10^{-5}$ μm s^{-1} (± s.e.m.; $n = 10$)) and a complete loss of response to high calcium (**Fig. 4e**). This result suggested that a drastic reduction of the side chain size at this position of the CSII essentially removes the gate altogether and eliminates calcium sensitivity. When Tyr149 was mutated to leucine (Y149L), the channels displayed only low permeabilities that were also unaffected by calcium ($P_f = 19.2 \times 10^{-5} \pm 1.2 \times 10^{-5}$ μm s^{-1} (± s.e.m.; $n = 10$) under low Ca^{2+} and $17.2 \times 10^{-5} \pm 0.8 \times 10^{-5}$ μm s^{-1} (± s.e.m.; $n = 10$) under high Ca^{2+}) (**Fig. 4e**), thus suggesting that substitution with a large hydrophobic side chain restricts channel gating and consequently abolishes Ca^{2+}–CaM modulation. Lastly, we mutated Tyr149 to serine (Y149S) because we hypothesized that the hydroxyl group that it has in common with tyrosine might be important for the gating mechanism. The Y149S mutant resulted in water permeability rates that were comparable to those of wild-type channels under low-calcium conditions ($P_f = 35.7 \times 10^{-5} \pm 6.1 \times 10^{-5}$ μm s^{-1} (± s.e.m.; $n = 10$)) and displayed marginal reduction (~30%) in permeability rates under high calcium ($P_f = 24.4 \times 10^{-5} \pm 5.3 \times 10^{-5}$ μm s^{-1} (± s.e.m.; $n = 10$)) (**Fig. 4e**), thus suggesting that serine can partially mimic the gating mechanism mediated by Tyr149.

These experimental data are consistent with our molecular dynamics–based results suggesting that the AQP0 CSII residue Tyr149 alters both the magnitude of the water permeability and its calcium modulation. The data also demonstrate that Tyr149 serves as a dynamic channel gate that allosterically couples Ca^{2+}–CaM binding at the AQP0 C terminus to water-channel closure at CSII.

DISCUSSION

Calmodulin regulates the activity of numerous membrane channels in response to changes in intracellular Ca^{2+} concentration. Despite this central role in channel regulation, very little is known about the underlying structural and molecular mechanisms by which CaM modulates channel function. In this study, we used hybrid methods to determine the pseudoatomic structure of the AQP0 water channel in complex with CaM, providing the first complete structural model for any full-length membrane channel in complex with CaM.

The resulting AQP0–CaM structure shows the AQP0 tetramer in complex with two CaM molecules. We were able to obtain mechanistic insight into CaM regulation, using molecular dynamics simulations, which showed that CaM binding to the AQP0 C terminus allosterically modulates the dynamics at the CSII pore constriction site, thus resulting in channel closure. The bridging of CaM across two neighboring subunits of AQP0 provides a mechanical force, or tension, that acts on the dynamics of the AQP0 CSII. Our molecular dynamics analysis shows that the stabilizing effect of CaM binding at the AQP0 C terminus is propagated over ~15–20 Å to the CSII site through the cytoplasmic linker and the last transmembrane helix of each channel (**Fig. 3**). This allosteric mechanism was experimentally supported by mutagenesis and functional studies that showed that CaM regulation of AQP0 water permeability is effectively blocked when the CSII gating residue Tyr149 is mutated. Together, our results show that CaM binding at the AQP0 C terminus is communicated to the CSII gate through allosteric interactions that favor a closed conformation, thereby dynamically modulating water permeability in a Ca^{2+}-dependent manner (**Fig. 5**).

We demonstrated that CaM binds full-length AQP0 with a 2:1 (AQP0/CaM) stoichiometry, using chemical cross-linking, structural EM analysis and ITC binding studies (**Figs. 1** and **2**), confirming previous studies using NMR spectroscopy[35]. In the AQP0 structure, the only way to facilitate this type of interaction is for two α-helical CaM-binding domains from neighboring subunits to come together in an antiparallel orientation[35]. On the basis of these results, we have proposed a stepwise bind-and-capture mechanism used by CaM to assemble the 2:1 AQP0–CaM complex (**Fig. 2f**). There are currently only two high-resolution structures of CaM bridging two α-helical peptides, belonging to the ptGAD–CaM complex[45] and the $Ca_{V1.2}$–CaM complex[46,47]. In either case, the CaM-binding domains adopt antiparallel α-helical orientations that intersect similarly to other dimeric coiled-coil interactions. In the ptGAD–CaM complex, a single CaM wraps around the intersection of the ptGAD dimer in a compact conformation. Unlike the stepwise association with AQP0, CaM appears to bind both ptGAD α-helices simultaneously[53].

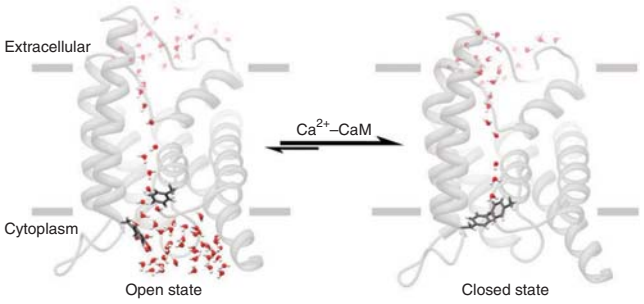

Figure 5 Mechanism of Ca^{2+}–CaM regulation of AQP0. The AQP0 water channel exists in equilibrium between an open state (left) and closed state (right). These states are formed by dynamic conformational changes at the CSII formed by residues Tyr149, Phe75 and His66. Binding of Ca^{2+}–CaM at the C terminus of AQP0 results in a shift in this equilibrium by allosteric stabilization of the closed CSII state, thereby restricting water-channel permeability. The structural models were obtained from the molecular dynamics simulations. AQP0 is shown as gray ribbon, and water molecules are shown in red. Some water molecules were deleted in the figure for display purposes and clarity. Likewise, the last transmembrane helix of AQP0 is removed for clarity. CSII residues Tyr149 and Phe75 are shown as stick representations.

In the $Ca_{V1.2}$–CaM complex, two CaM molecules bind a $Ca_{V1.2}$ helical dimer, with each CaM adopting an extended conformation that bridges the $Ca_{V1.2}$ dimer distant from the helical intersection. Our EM data suggested that the interaction of AQP0 with CaM was most consistent with that of the compact ptGAD–CaM complex. Although our structural studies suggest that the AQP0-CaM interaction is similar to the ptGAD-CaM interaction, the regulatory mechanisms are quite different. For ptGAD, CaM binding relieves an autoinhibitory domain of the enzyme, thus resulting in functional activation[54]. For AQP0, CaM binding induces allosteric changes in the channel gate that restrict water permeation. In both cases, a 2:1 stoichiometry may provide a more economical use of CaM. However, for AQP0 this stoichiometry is thought to have an important functional role in the regulatory mechanism.

CaM binding to two neighboring AQP0 C-terminal domains stabilizes the cytoplasmic region of the channel, including the CSII gate. The AQP0 C termini can be thought of as the reins of the channel through which Ca^{2+}–CaM provides the mechanical force to restrain the channel gate and stabilize the channel in its closed state (**Fig. 5**). This may be similar to the mechanisms used to regulate other channels whose gating properties are modulated by CaM, such as the small conductance potassium (SK) channel[55]. Crystallographic studies of the C-terminal domain from the SK channel bound to CaM in the presence or absence of Ca^{2+} revealed conformational changes that were proposed to drive the activation of the SK channel in a Ca^{2+}-dependent manner[36,56]. Ca^{2+}-free CaM is constitutively associated with a C-terminal domain of SK channels in a 1:1 stoichiometry. When CaM binds Ca^{2+}, it associates with an additional SK-channel domain from a neighboring subunit to form a 2:2 complex, thus resulting in a unique structure with CaM extended across three α-helices[36]. This Ca^{2+}-induced interaction was proposed to rotate the C-terminal domain of the SK channel and provide the mechanical force required to open the channel gate[36,56]. Many other channels may use similar CaM-driven cooperativity to regulate their functions. For example, the NR1 subunits of the NMDA receptor bind CaM with a 2:1 stoichiometry to result in channel inactivation[57]. Although there is currently no structural information on this complex, it is conceivable that this is another case in which the stoichiometry provides the mechanical force used to allosterically drive channel closure.

Unlike other multimeric channels, such as ion channels, cooperativity between AQP subunits is not a functional requirement because each monomer forms its own fully active water pore[58]. Our studies suggest that AQP0 tetramerization is a prerequisite for the binding of regulatory proteins such as Ca^{2+}–CaM. Thus, AQP0 tetramerization appears to provide the necessary scaffold that facilitates cooperative regulatory interactions between subunits. Facilitating cooperativity between neighboring subunits may prove to be a common theme used by CaM to modulate the functions of membrane channels. This possibility emphasizes the need to structurally and mechanistically characterize these interactions in full-length channels. Future studies using complementary structural biology techniques, such as those applied here, will undoubtedly unveil new and unexpected mechanisms used by CaM to regulate its many membrane-channel targets.

METHODS

Methods and any associated references are available in the online version of the paper.

Accession codes. The EM map has been deposited with the EM database (EMD-5679). The pseudoatomic model of the AQP0–CaM complex fit to the EM density has been deposited with the Protein Data Bank (PDB 3J41).

Note: Any Supplementary Information and Source Data files are available in the online version of the paper.

ACKNOWLEDGMENTS

The authors would like to thank M. Sarhan (Howard Hughes Medical Institute (HHMI), Janelia Farm Research Campus) for help with ITC and D. Shi (HHMI, Janelia Farm Research Campus) for help with various aspects of EM. Research in the laboratory of J.E.H. is supported by US National Institutes of Health (NIH) National Eye Institute grant EY5661 (J.E.H.). Research by D.M.C. was supported by the NIH National Library of Medicine Biomedical Informatics Research Training Program Award, no. LM007443. Research by S.L.R. was supported by the Ruth L. Kirschtein National Research Service Award from NIH. Research in the laboratory of D.J.T. is supported by NIH National Institute of Neurological Disorders–National Institute of General Medical Sciences grant GM86685 and US National Science Foundation grant CHE-0750175 (D.J.T.). M.H. is supported by a fellowship from the German Academy of Sciences Leopoldina. This work was supported in part by NIH grant R01 GM079233 (T.G.). Research in the laboratory of T.G. is funded by the HHMI (T.G.).

AUTHOR CONTRIBUTIONS

S.L.R., D.M.C., J.E.H. and T.G. conceived of and designed the experiments for this work. All authors contributed to data analysis and preparation of the manuscript. S.L.R. performed protein purification, EM and ITC binding studies on the AQP0–CaM complexes. D.M.C., J.A.F., M.H. and D.J.T. performed setup and analysis of molecular dynamics simulations. D.M.C. and K.L.N.-C. performed oocyte permeability measurements, construction of oocyte expression constructs and analysis of oocyte permeability data.

COMPETING FINANCIAL INTERESTS

The authors declare no competing financial interests.

1. Saimi, Y. & Ling, K.Y. Calmodulin activation of calcium-dependent sodium channels in excised membrane patches of *Paramecium*. *Science* **249**, 1441–1444 (1990).
2. Zühlke, R.D., Pitt, G.S., Deisseroth, K., Tsien, R.W. & Reuter, H. Calmodulin supports both inactivation and facilitation of L-type calcium channels. *Nature* **399**, 159–162 (1999).
3. Tan, H.L. *et al.* A calcium sensor in the sodium channel modulates cardiac excitability. *Nature* **415**, 442–447 (2002).
4. Saimi, Y. & Kung, C. Calmodulin as an ion channel subunit. *Annu. Rev. Physiol.* **64**, 289–311 (2002).
5. Meissner, G. Evidence of a role for calmodulin in the regulation of calcium release from skeletal muscle sarcoplasmic reticulum. *Biochemistry* **25**, 244–251 (1986).
6. Smith, J.S., Rousseau, E. & Meissner, G. Calmodulin modulation of single sarcoplasmic reticulum Ca^{2+}-release channels from cardiac and skeletal muscle. *Circ. Res.* **64**, 352–359 (1989).
7. Zalk, R., Lehnart, S.E. & Marks, A.R. Modulation of the ryanodine receptor and intracellular calcium. *Annu. Rev. Biochem.* **76**, 367–385 (2007).
8. Scott, K., Sun, Y., Beckingham, K. & Zuker, C.S. Calmodulin regulation of *Drosophila* light-activated channels and receptor function mediates termination of the light response *in vivo*. *Cell* **91**, 375–383 (1997).
9. Zhang, Z. *et al.* Activation of Trp3 by inositol 1,4,5-trisphosphate receptors through displacement of inhibitory calmodulin from a common binding domain. *Proc. Natl. Acad. Sci. USA* **98**, 3168–3173 (2001).
10. Zhu, M.X. Multiple roles of calmodulin and other Ca^{2+}-binding proteins in the functional regulation of TRP channels. *Pflugers Arch.* **451**, 105–115 (2005).
11. Peracchia, C., Sotkis, A., Wang, X.G., Peracchia, L.L. & Persechini, A. Calmodulin directly gates gap junction channels. *J. Biol. Chem.* **275**, 26220–26224 (2000).
12. Sotkis, A. *et al.* Calmodulin colocalizes with connexins and plays a direct role in gap junction channel gating. *Cell Commun. Adhes.* **8**, 277–281 (2001).
13. Peracchia, C. Chemical gating of gap junction channels; roles of calcium, pH and calmodulin. *Biochim. Biophys. Acta* **1662**, 61–80 (2004).
14. Németh-Cahalan, K.L. & Hall, J.E. pH and calcium regulate the water permeability of aquaporin 0. *J. Biol. Chem.* **275**, 6777–6782 (2000).
15. Varadaraj, K., Kumari, S., Shiels, A. & Mathias, R.T. Regulation of aquaporin water permeability in the lens. *Invest. Ophthalmol. Vis. Sci.* **46**, 1393–1402 (2005).
16. Babu, Y.S. *et al.* Three-dimensional structure of calmodulin. *Nature* **315**, 37–40 (1985).
17. Zhang, M., Tanaka, T. & Ikura, M. Calcium-induced conformational transition revealed by the solution structure of apo calmodulin. *Nat. Struct. Biol.* **2**, 758–767 (1995).

18. Kuboniwa, H. *et al.* Solution structure of calcium-free calmodulin. *Nat. Struct. Biol.* **2**, 768–776 (1995).
19. Chou, J.J., Li, S., Klee, C.B. & Bax, A. Solution structure of Ca^{2+}–calmodulin reveals flexible hand-like properties of its domains. *Nat. Struct. Biol.* **8**, 990–997 (2001).
20. Vogel, H.J. The Merck Frosst Award Lecture 1994. Calmodulin: a versatile calcium mediator protein. *Biochem. Cell Biol.* **72**, 357–376 (1994).
21. Yamniuk, A.P. & Vogel, H.J. Calmodulin's flexibility allows for promiscuity in its interactions with target proteins and peptides. *Mol. Biotechnol.* **27**, 33–57 (2004).
22. Gonen, T. & Walz, T. The structure of aquaporins. *Q. Rev. Biophys.* **39**, 361–396 (2006).
23. Murata, K. *et al.* Structural determinants of water permeation through aquaporin-1. *Nature* **407**, 599–605 (2000).
24. de Groot, B.L., Frigato, T., Helms, V. & Grubmuller, H. The mechanism of proton exclusion in the aquaporin-1 water channel. *J. Mol. Biol.* **333**, 279–293 (2003).
25. Bloemendal, H., Zweers, A., Vermorken, F., Dunia, I. & Benedetti, E.L. The plasma membranes of eye lens fibres. Biochemical and structural characterization. *Cell Differ.* **1**, 91–106 (1972).
26. Németh-Cahalan, K.L., Kalman, K. & Hall, J.E. Molecular basis of pH and Ca^{2+} regulation of aquaporin water permeability. *J. Gen. Physiol.* **123**, 573–580 (2004).
27. Mulders, S.M. *et al.* Water channel properties of major intrinsic protein of lens. *J. Biol. Chem.* **270**, 9010–9016 (1995).
28. Chandy, G., Zampighi, G.A., Kreman, M. & Hall, J.E. Comparison of the water transporting properties of MIP and AQP1. *J. Membr. Biol.* **159**, 29–39 (1997).
29. Harries, W.E., Akhavan, D., Miercke, L.J., Khademi, S. & Stroud, R.M. The channel architecture of aquaporin 0 at a 2.2-A resolution. *Proc. Natl. Acad. Sci. USA* **101**, 14045–14050 (2004).
30. Gonen, T. *et al.* Lipid-protein interactions in double-layered two-dimensional AQP0 crystals. *Nature* **438**, 633–638 (2005).
31. Bok, D., Dockstader, J. & Horwitz, J. Immunocytochemical localization of the lens main intrinsic polypeptide (MIP26) in communicating junctions. *J. Cell Biol.* **92**, 213–220 (1982).
32. Costello, M.J., McIntosh, T.J. & Robertson, J.D. Distribution of gap junctions and square array junctions in the mammalian lens. *Invest. Ophthalmol. Vis. Sci.* **30**, 975–989 (1989).
33. Gonen, T., Sliz, P., Kistler, J., Cheng, Y. & Walz, T. Aquaporin-0 membrane junctions reveal the structure of a closed water pore. *Nature* **429**, 193–197 (2004).
34. Girsch, S.J. & Peracchia, C. Calmodulin interacts with a C-terminus peptide from the lens membrane protein MIP26. *Curr. Eye Res.* **10**, 839–849 (1991).
35. Reichow, S.L. & Gonen, T. Noncanonical binding of calmodulin to aquaporin-0: implications for channel regulation. *Structure* **16**, 1389–1398 (2008).
36. Schumacher, M.A., Rivard, A.F., Bachinger, H.P. & Adelman, J.P. Structure of the gating domain of a Ca^{2+}-activated K^+ channel complexed with Ca^{2+}/calmodulin. *Nature* **410**, 1120–1124 (2001).
37. Van Petegem, F., Chatelain, F.C. & Minor, D.L. Jr. Insights into voltage-gated calcium channel regulation from the structure of the CaV1.2 IQ domain–Ca^{2+}/calmodulin complex. *Nat. Struct. Mol. Biol.* **12**, 1108–1115 (2005).
38. Mori, M.X., Vander Kooi, C.W., Leahy, D.J. & Yue, D.T. Crystal structure of the Ca_V2 IQ domain in complex with Ca^{2+}/calmodulin: high-resolution mechanistic implications for channel regulation by Ca^{2+}. *Structure* **16**, 607–620 (2008).
39. Sarhan, M.F., Tung, C.C., Van Petegem, F. & Ahern, C.A. Crystallographic basis for calcium regulation of sodium channels. *Proc. Natl. Acad. Sci. USA* **109**, 3558–3563 (2012).
40. Samsó, M. & Wagenknecht, T. Apocalmodulin and Ca^{2+}-calmodulin bind to neighboring locations on the ryanodine receptor. *J. Biol. Chem.* **277**, 1349–1353 (2002).
41. Huang, X., Fruen, B., Farrington, D.T., Wagenknecht, T. & Liu, Z. Calmodulin-binding locations on the skeletal and cardiac ryanodine receptors. *J. Biol. Chem.* **287**, 30328–30335 (2012).
42. Frank, J. *et al.* SPIDER and WEB: processing and visualization of images in 3D electron microscopy and related fields. *J. Struct. Biol.* **116**, 190–199 (1996).
43. Grigorieff, N. FREALIGN: high-resolution refinement of single particle structures. *J. Struct. Biol.* **157**, 117–125 (2007).
44. Pettersen, E.F. *et al.* UCSF Chimera: a visualization system for exploratory research and analysis. *J. Comput. Chem.* **25**, 1605–1612 (2004).
45. Yap, K.L., Yuan, T., Mal, T.K., Vogel, H.J. & Ikura, M. Structural basis for simultaneous binding of two carboxy-terminal peptides of plant glutamate decarboxylase to calmodulin. *J. Mol. Biol.* **328**, 193–204 (2003).
46. Fallon, J.L. *et al.* Crystal structure of dimeric cardiac L-type calcium channel regulatory domains bridged by Ca^{2+}* calmodulins. *Proc. Natl. Acad. Sci. USA* **106**, 5135–5140 (2009).
47. Kim, E.Y. *et al.* Multiple C-terminal tail Ca^{2+}/CaMs regulate $Ca_V1.2$ function but do not mediate channel dimerization. *EMBO J.* **29**, 3924–3938 (2010).
48. Smart, O.S., Neduvelil, J.G., Wang, X., Wallace, B.A. & Sansom, M.S. HOLE: a program for the analysis of the pore dimensions of ion channel structural models. *J. Mol. Graph.* **14**, 354–360, 376 (1996).
49. Jensen, M.Ø. & Mouritsen, O.G. Single-channel water permeabilities of *Escherichia coli* aquaporins AqpZ and GlpF. *Biophys. J.* **90**, 2270–2284 (2006).
50. Jensen, M.Ø. *et al.* Dynamic control of slow water transport by aquaporin 0: implications for hydration and junction stability in the eye lens. *Proc. Natl. Acad. Sci. USA* **105**, 14430–14435 (2008).
51. Hashido, M., Ikeguchi, M. & Kidera, A. Comparative simulations of aquaporin family: AQP1, AQPZ, AQP0 and GlpF. *FEBS Lett.* **579**, 5549–5552 (2005).
52. Yang, B. & Verkman, A.S. Water and glycerol permeabilities of aquaporins 1–5 and MIP determined quantitatively by expression of epitope-tagged constructs in *Xenopus* oocytes. *J. Biol. Chem.* **272**, 16140–16146 (1997).
53. Yuan, T. & Vogel, H.J. Calcium-calmodulin-induced dimerization of the carboxyl-terminal domain from petunia glutamate decarboxylase: a novel calmodulin-peptide interaction motif. *J. Biol. Chem.* **273**, 30328–30335 (1998).
54. Gut, H. *et al.* A common structural basis for pH- and calmodulin-mediated regulation in plant glutamate decarboxylase. *J. Mol. Biol.* **392**, 334–351 (2009).
55. Xia, X.M. *et al.* Mechanism of calcium gating in small-conductance calcium-activated potassium channels. *Nature* **395**, 503–507 (1998).
56. Schumacher, M.A., Crum, M. & Miller, M.C. Crystal structures of apocalmodulin and an apocalmodulin/SK potassium channel gating domain complex. *Structure* **12**, 849–860 (2004).
57. Wang, C., Wang, H.G., Xie, H. & Pitt, G.S. Ca^{2+}/CaM controls Ca^{2+}-dependent inactivation of NMDA receptors by dimerizing the NR1 C termini. *J. Neurosci.* **28**, 1865–1870 (2008).
58. Shi, L.B., Skach, W.R. & Verkman, A.S. Functional independence of monomeric CHIP28 water channels revealed by expression of wild-type mutant heterodimers. *J. Biol. Chem.* **269**, 10417–10422 (1994).

ONLINE METHODS

Cross-linking and purification of the AQP0–CaM complex. The native full-length aquaporin-0 (AQP0) was purified from lenses obtained from young sheep, and the vertebrate calmodulin (CaM) was heterologously expressed in *E. coli* and purified as previously described[35]. CaM was prepared at 8 mg ml^{-1} in activation buffer containing 25 mM MES, pH 6.0, and 5 mM $CaCl_2$. The activation reaction was performed with 10 mM 1-ethyl-3-(3-dimethylaminopropyl) carbodiimide (EDC, Pierce) and 20 mM *N*-hydroxysulfosuccinimide (sulfo-NHS, Pierce). The activation reaction was allowed to proceed at room temperature for 15 min, and unreacted EDC was quenched with 20 mM β-mercaptoethanol (βMe). Activated CaM (2 mg ml^{-1}) was added to freshly purified AQP0 (1.5 mg ml^{-1}) (corresponding to a 2× molar excess of CaM) in cross-linking buffer containing 25 mM HEPES, pH 7.4, 5 mM $CaCl_2$, 5 mM βMe and 0.3% decylmaltoside (DM). The cross-linking reaction was allowed to proceed for 90 min at room temperature and was quenched by the addition of 10 mM hydroxylamine (Sigma) and placed on ice. The reaction mixture was loaded onto an anion-exchange column (Capto adhere, GE Lifescience) equilibrated with 20 mM HEPES, pH 5.5, 1 mM $CaCl_2$ and 0.3% DM. Unreacted AQP0 was separated from the AQP0–CaM cross-linked product by application of a gradient of 750 mM NaCl. The eluted AQP0–CaM cross-linked complex was further purified from excess CaM by size-exclusion chromatography (S200, GE Lifescience) pre-equilibrated with buffer containing 25 mM HEPES, pH 7.4, 5 mM $CaCl_2$ and 0.3% DM. SDS-PAGE and silver staining was used to monitor each step of the purification (**Supplementary Fig. 1**). The absence of a 2:2 AQP0–CaM cross-linked complex or other higher-molecular-weight aggregates in SDS-PAGE demonstrates that the 2:1 stoichiometric complex of AQP0–CaM was specifically stabilized by the EDC reaction. Protein concentrations were determined by BCA assay (Pierce) or UV absorbance at 280 nm.

Electron microscopy and three-dimensional reconstruction. The freshly purified AQP0–CaM complex was diluted to 0.02 mg ml^{-1} with buffer containing 25 mM HEPES, pH 7.4, 5 mM $CaCl_2$ and 0.3% DM. A volume of 2 µl was applied to a 400 mesh carbon-coated EM grid (Ted Pella), stained with uranyl formate (0.75% w/v), blotted on filter paper and dried by laminar air flow. Negatively stained particles were visualized on a 120 kV TEM (FEI), and images were recorded at a nominal magnification of ×52,000 at the specimen level on film (Kodak SO-163) as tilted-pair images (α of 0° and 50°). Images were digitized with a Nikon Coolscan 9000 with a 6.9-µm step size and binned three times to yield a final pixel size of 3.98 Å per pixel. Thon rings in the power spectra were used to select only those micrographs free of drift or noticeable astigmatism. The contrast transfer function (CTF) parameters were determined for each micrograph with CTFTILT[59]. Subsequently, 11,720 particles were selected and processed in SPIDER[42] for generation of multivariate reference-free projection averages and initial three-dimensional (3D) reconstruction with random conical tilt methods. Final refinement of the 3D density map was performed with FREALIGN[43]. The final 3D density map was reconstructed with C2 symmetry and filtered to 25-Å resolution, as suggested by Fourier shell correlation (FSC) analysis.

Molecular modeling of the AQP0–CaM complex. A pseudoatomic model of the AQP0–CaM complex was built by initially docking available crystal structures into the AQP0–CaM EM density map as follows and in **Supplementary Figure 2**. The transmembrane domain of the bovine AQP0 crystal structure (PDB 2B6P, residues 9–222)[30] was manually placed into the 65 × 65 × 40–Å region of the EM map with the cytoplasmic face of the AQP0 tetramer facing the two vacant lobe domains of the EM map. This initial placement was rotationally and translationally optimized by computational minimization routines in Chimera[44]. The structure of Ca^{2+}–CaM bound to the plant glutamate decarboxylase peptides (ptGAD–CaM, PDB 1NWD)[45] was manually placed within the two vacant lobes of the EM map in a symmetric fashion, with the CaM binding clefts facing the AQP0 tetramer. The structure of CaM bound to the voltage-gated calcium channel ($Ca_{V1.2}$)–CaM complex[46,47] was also assessed for fitting into the EM map; however, CaM adopts an extended conformation in the $Ca_{V1.2}$–CaM complex that was inconsistent with the dimensions of our EM reconstruction. The helical axes of the two ptGAD subunits were oriented toward the cytoplasmic ends of the last transmembrane helix of neighboring AQP0 monomers. This placement was optimized to avoid steric clashes with AQP0. The two ptGAD α-helical subunits were used as templates to model the AQP0 C-terminal helices from each subunit (residues 227–241). The C-terminal AQP0 α-helical residues Leu234 and Leu237 were structurally aligned with the ptGAD hydrophobic anchoring residues Trp485 and Ile482, respectively. The cytoplasmic linkers connecting the AQP0 C-terminal helices to the last transmembrane helix of each subunit (residues 223–226) were manually built and minimized with COOT[60]. The CaM molecules and the AQP0 C-terminal linker and CaM binding domains (residues 223–241) were subjected to steepest decent minimization and subsequent conjugate gradient minimization routines in Chimera to regularize the geometries and remove steric interactions. A map calculated at 25 Å (σ = 3.5) corresponding to the final model gave a cross-correlation of 0.95 compared to that of the experimental map (σ = 4.96) in Chimera.

Isothermal titration calorimetry. ITC experiments were performed on a MicroCal VP-ITC (GE Lifescience). AQP0^{CBD} peptides corresponding to the wild-type bovine sequence (residues 223–242) or the point mutants L227A, V230A, L234A, I236A or L237A were synthesized and purified to >98% purity (Biomatik). The AQP0^{CBD} peptides and CaM were dialyzed against 20 mM HEPES, pH 7.0 and 5 mM $CaCl_2$ over 72 h with a 1,000-Da molecular-weight cutoff membrane (Spectra/Por). AQP0^{CBD} peptide concentrations were adjusted to 500 µM and titrated into the MicroCal cell containing Ca^{2+}–CaM at 20 µM or dialysis buffer only and held at 25 °C. ITC data were processed in Origin (OriginLab) by subtraction of the background heats of peptide mixing to buffer alone from heats obtained from mixing with Ca^{2+}–CaM, and thermodynamic parameters were obtained by fitting the data to a two-state binding isotherm.

Molecular dynamics simulations. Two simulation systems were generated for POPC-embedded AQP0: one for AQP0 in complex with CaM and one for AQP0 alone (CaM free). The AQP0–CaM complex system was constructed similarly to the structure presented in **Figure 1**, with PDB 2B6P for AQP0 (residues 5 to 239) and PDB 1NWD for CaM. The complex in our simulations consisted of one AQP0 tetramer, two CaM molecules, 8 Ca^{2+} ions, 410 POPC molecules and 56,701 waters, for a total of 244,011 atoms. For the CaM–free system, a starting conformation of the AQP0 tetramer (residues 5–239) in the absence of CaM was created by deletion of the CaM coordinates from the AQP0–CaM complex. In this way, the starting conformations of AQP0 in the two simulations were identical. In both systems, the CSII sites of AQP0 were unaltered from the original PDB 2B6P model (**Supplementary Fig. 4**). The simulation for the CaM-free system included the AQP0 tetramer, 410 POPC molecules, 40,175 waters and 32 counterions, for a total of 189,933 atoms. These starting configurations were minimized by 1,000 steps of conjugate-gradient energy minimization followed by 4 ns of simulation at constant temperature (300 K) and volume with the protein backbone atoms held fixed. The protein backbone atoms were then released in a stepwise manner over 4 ns. Unrestrained simulations were run at constant temperature and pressure (1 atm) for 560 ns for the AQP0–CaM complex and 495 ns for the apo-AQP0 system.

The simulations were performed with the NAMD 2.7b1 (ref. 61). The CHARMM22 and CHARMM32 force fields[62,63] were used for protein and lipids, respectively, and the TIP3P model was used for water[64]. The smooth particle mesh Ewald method[65] was used to calculate electrostatic interactions. Short-range real-space interactions were cut off at 12 Å, with a switching function. A reversible multiple-time-step algorithm[66] was used to integrate the equations of motion with a time step of 4 fs for electrostatic forces, 2 fs for short-range non-bonded forces and 1 fs for bonded forces. All bond lengths involving hydrogen atoms were held fixed. A Langevin dynamics scheme was used for temperature control, and a Noseì–Hoover–Langevin piston was used for pressure control[67,68]. Molecular graphics and trajectory analyses were performed with VMD 1.8.7 (ref. 69) over the last 519 ns (AQP0–CaM system) or 474 ns (CaM-free system) of each trajectory. Water permeabilities were calculated with a method described previously[49] and implemented in VMD using tcl. In brief, the pore was defined and waters within the pore selected, the velocities of these waters were calculated while they remained in the pore, and the process was repeated over the equilibrated portion of the trajectories. The resultant collective coordinate for each trajectory was converted to a collective diffusion constant, which was then converted to the single-channel osmotic permeability constant. Statistics, where shown, were calculated as the average ± s.e.m. of the four pores from each trajectory. Pore profile analysis was performed with HOLE[48].

Water permeability assays. Oocytes from *Xenopus laevis* were obtained from Ecocyte and injected with 10 ng of RNA encoding wild-type, Y149G, Y149L

or Y149S AQP0 generated with the mMessage mMachine T3 kit (Ambion/Life Technologies) as described previously[14,26]. Water permeability was calculated from the rate of volume increase, which was estimated from automated measurements of the increase in cross-sectional area of the oocyte in response to a dilution of ND96. Swelling rates due to water flow were estimated from measurements of the cross-sectional area of the osmotically challenged oocytes as a function of time. The cross-sectional area was measured as a function of time for acquisition of images of the oocyte at appropriate time intervals (on the order of a few seconds). The number of pixels in the oocyte cross-section was calculated automatically by ImageJ and transferred to an Excel spreadsheet in which pixel number was converted to area with the scale factors of the microscope measured from a stage micrometer. These cross-sectional data were used to calculate volume as the 3/2 power of area. From these estimates of volume as a function of time, we calculated permeability, an intrinsic property of the membrane, from the formula $P_f = [d(V/V_o)/dt][V_o/S_o]/[\Delta_{osm} V_w]$. V is the volume as a function of time, V_o is the volume at time 0, S_o is the estimated geometric surface area of the oocyte at time 0, Δ_{osm} is the osmotic gradient and V_w is the partial molar volume of water. The initial slope of the $V_{(t)}$ curve was used to determine the value of $d(V/V_o)/dt$ in the formula above. Thus P_f is directly proportional to the observed initial swelling rate. Total membrane expression levels were assayed by western blot after isolation of plasma-membrane proteins with the ProteoExtract Native Membrane Protein Extraction Kit (Calbiochem/EMD Millipore). The uncropped gel in **Figure 4** is shown in **Supplementary Figure 5**. Each sample (corresponding to approximately half an oocyte) was separated on a NuPAGE 4–12% Bis-Tris gel (Life Technologies) and transferred to PVDF (Life Technologies) for 1 h at 100 V. Levels of AQP0 abundance were probed with an AQP0 primary antibody (1:500 Santa Cruz Biotech AQP0 (H-44) rabbit polyclonal IgG; sc-99059) followed by a secondary antibody (1:10,000 Promega anti-Rabbit IgG HRP; cat. no. W4011), detected with a Super Signal West Femto kit (Thermo) and exposed on a Fuji LAS-4000 gel documentation system. We note that the accurate assessments of protein abundance from immunoblots can be problematic.

59. Mindell, J.A. & Grigorieff, N. Accurate determination of local defocus and specimen tilt in electron microscopy. *J. Struct. Biol.* **142**, 334–347 (2003).
60. Emsley, P. & Cowtan, K. Coot: model-building tools for molecular graphics. *Acta Crystallogr. D Biol. Crystallogr.* **60**, 2126–2132 (2004).
61. Phillips, J.C. *et al.* Scalable molecular dynamics with NAMD. *J. Comput. Chem.* **26**, 1781–1802 (2005).
62. MacKerell, A.D. *et al.* All-atom empirical potential for molecular modeling and dynamics studies of proteins. *J. Phys. Chem. B* **102**, 3586–3616 (1998).
63. Klauda, J.B., Brooks, B.R., MacKerell, A.D. Jr., Venable, R.M. & Pastor, R.W. An *ab initio* study on the torsional surface of alkanes and its effect on molecular simulations of alkanes and a DPPC bilayer. *J. Phys. Chem. B* **109**, 5300–5311 (2005).
64. Jorgensen, W.L., Chandrasekhar, J., Madura, J.D., Impey, R.W. & Klein, M.L. Comparison of simple potential functions for simulating liquid water. *J. Chem. Phys.* **79**, 926–935 (1983).
65. Essmann, U. *et al.* A smooth particle mesh Ewald method. *J. Chem. Phys.* **103**, 8577–8593 (1995).
66. Grubmuller, H., Heller, H., Windermuth, A. & Schulten, K. Generalized Verlet algorithm for efficient molecular dynamics simulations with long-range interactions. *Mol. Simul.* **6**, 121–142 (1991).
67. Martyna, G.J., Tobiax, D.J. & Klein, M.L. Constant pressure molecular dynamics algorithms. *J. Chem. Phys.* **101**, 4177–4189 (1994).
68. Feller, S.E., Zhang, Y., Pastor, R.W. & Brooks, B.R. Constant pressure molecular dynamics simulation: The Langevin piston method. *J. Chem. Phys.* **103**, 4613–4621 (1995).
69. Humphrey, W., Dalke, A. & Schulten, K. VMD: visual molecular dynamics. *J Mol. Graph.* **14**, 33–38 (1996).

doi:10.1038/nsmb.2630